Surface studies of phase formation in Co–Ge system: Reactive deposition epitaxy versus solid-phase epitaxy

I. Goldfarb[a)]
Department of Solid Mechanics, Materials and Systems, The Fleischman Faculty of Engineering, Tel Aviv University, Ramat Aviv 69978, Israel

G.A.D. Briggs
Department of Materials, University of Oxford, Parks Road, Oxford OX1 3PH, United Kingdom

(Received 25 May 2000; accepted 20 December 2000)

Morphological evolution of cobalt germanide epilayers, Co_xGe_y, was investigated *in situ* by scanning tunneling microscopy and spectroscopy and reflection high-energy electron diffraction, as a function of deposition method and, hence, the phase content of the epilayer. During reactive deposition epitaxy, in which Co atoms were evaporated onto a flat pseudomorphic Ge/Si(001) wetting layer at 773 K, the first phase formed was cobalt digermanide, $CoGe_2$, in the form of elongated pyramidal islands. Each of these three-dimensional islands has locally exerted an additional strain on the Ge wetting layer already strained at the Ge/Si(001) interface, lifting the layer metastability and causing, in turn, the formation of three-dimensional Ge pyramids underneath every $CoGe_2$ island. Solid-phase epitaxy of Co onto the same Ge/Si(001) epilayer resulted in the formation of more Co-rich germanide islands. Coupling of strain from these germanides to the epitaxial Ge/Si(001) strain has also facilitated a two-dimensional-to-three-dimensional transition of the Ge layer, however, with the germanide islands located at the Ge pyramid troughs, rather than crests. The difference in the relative location of germanide and germanium islands in these two cases is explained by accommodation of the large lattice-constant germanides at the more relaxed regions of the Ge pyramid crests and the smaller lattice-constant at the compressed Ge pyramid troughs.

I. INTRODUCTION

The interest in cobalt germanides, in particular $CoGe_2$, stems from the fact that they can be used as a contact material for $Si_{1-x}Ge_x$ alloys and GaAs, and as infrared detectors.[1–5] Although there is a considerable amount of literature on crystallography, microstructure, phase formation, and electronic properties of various cobalt silicides due to their potential as self-aligned silicides, there are relatively few publications concerning structure and properties of cobalt germanides. The data are incomplete and controversial. This is partly due to the complexity of the Co–Ge system and the different methods of germanide synthesis used by various groups.[1–7] In addition, because of the importance of contacts to $Si_{1-x}Ge_x$ alloys, some groups investigate the reaction of Co with $Si_{1-x}Ge_x$, rather than Ge, layers, which adds complexity to the understanding of germanide formation kinetics.[8–14] The equilibrium bulk-phase diagram contains seven phases[15]: cubic Co_3Ge, hexagonal Co_5Ge_2 (a = 3.93 Å, c = 5.01 Å), hexagonal β–Co_5Ge_3 and orthorhombic α–Co_5Ge_3, monoclinic (a = 11.65 Å, b = 3.81 Å, c = 4.95 Å) and cubic (a = 4.64 Å) CoGe, tetragonal Co_5Ge_7 (a = 7.64 Å, c = 5.81 Å), orthorhombic $CoGe_2$ ($a = b$ = 5.68 Å, c = 10.82 Å), and Pearson's Crystallographic Data contain also orthorhombic Co_2Ge (a = 5.02 Å, b = 3.82 Å, c = 7.26 Å).[16] Co_2Ge was found to form between Co and Ge layers after ion beam mixing by Dhar and Kulkarni.[4] Solid-phase epitaxy (SPE) of Co onto Ge/SiO_2 followed by a 673–723 K anneal resulted in the formation of CoGe, which was transformed into $CoGe_2$ on an additional 923–1023 K anneal.[5] Ashburn *et al.*[1] found Co_5Ge_7 and $CoGe_2$ in SPE of Co/Ge/Si(001) after a rapid thermal anneal (RTA) at 573 K and 698 K, respectively. Epitaxial $CoGe_2$/GaAs was obtained by simultaneous evaporation of Co and Ge^+ using partially ionized beam deposition at 1:2 flux ratio.[2,3] In addition to Co_5Ge_7 and $CoGe_2$, Co_3Ge_2 was observed to form in metal vapor vacuum arc cobalt implanted germanium.[6] Hence, α– and β–Co_5Ge_3 seem to appear only in the bulk form, whereas Co_3Ge_2 appears only during implantation. Diffusion

a) Address all correspondence to this author.
e-mail: ilang@eng.tau.ac.il

 © 2001 Materials Research Society

of Co through the Ge layer, with subsequent formation of $CoSi_2$ at the Ge/Si interface, i.e., Ge/$CoSi_2$/Si, has been witnessed, as well.[7]

Not only the phase type but also the phase morphology determine the metal-semiconductor compound layer properties. For example, although cobalt disilicide ($CoSi_2$) exhibits exceptional properties as a self-aligned silicide, the use of epitaxial $CoSi_2$ layers grown on Si(001) is impeded by misoriented three-dimensional (3D) crystallites.[17] To overcome this problem, the growth should take place on a vicinal Si(001) surface,[18] or a special "template" technique[19–23] should be used.

These two aspects, i.e., phase type and morphology, are not unrelated. Because each phase has its unique lattice constant, resulting from its crystalline structure and bonding, this affects the lattice mismatch with the underlying substrate. The elastic strain from this mismatch, combined with the relative surface and interface energies, may, in turn, influence the surface morphology of the growing layer.[24] We show that different morphologies of the cobalt germanide layers observed in our experiments correspond to different germanide phases and are the consequence of the optimal strain–relaxation by the growing layer in each case.

II. EXPERIMENT

The experiments were performed in a JEOL ultrahigh vacuum (UHV) elevated-temperature scanning tunneling microscope (STM), equipped with reflection high-energy electron diffraction (RHEED) and low-energy electron diffraction (LEED)–Auger spectrometer, and capable of operation up to 1500 K by resistive heating. Si(001) wafers were chemically treated *ex vacuo,* by repeated etch-and-regrowth procedure, to produce clean and homogeneous oxide at the top. In UHV (base pressure 1×10^{-8} Pa), after thorough degassing, this oxide was evaporated by repeated flashes at 1400 K, and the clean Si surface was left to order during a slow cool to the desired temperature (773 K in this case, measured by infrared pyrometer with ±30 K accuracy). Such treatment has generally proved effective in producing well-ordered (1×2) and (2×1) surfaces,[18,25–28] as was indeed verified this time by LEED and, after transferring the sample into the STM chamber, by RHEED and STM. The next step consisted of obtaining a flat and pseudomorphic Ge layer by gas source molecular-beam epitaxy (GSMBE) from GeH_4 to the maximal wetting layer thickness, namely, below the critical thickness for the Stranski-Krastanow transition. Ge growth was monitored in real time by continuous STM acquisition in a constant-current mode by using electrochemically etched W tips, as described elsewhere.[18,25–28] The growth was terminated the moment the $(M \times N)$ vacancy lines attained their minimum meander state, because further growth would have resulted in the formation of 3D Ge pyramids and huts.[25–29] The $(M \times N)$ surface mesh is formed by the intersection of N-periodic dimer vacancy lines (DVLs) with M-periodic dimer row vacancies (DRVs), in response to buildup of epitaxial strain in growing 2D Ge/Si(001) layers, as explained in detail elsewhere.[25–29] This critical thickness corresponded to approximately seven monolayers (7 ML), as determined by the deposition rate found from image subtraction at submonolayer coverages.[25,26] Hence, Co, supplied from a water-cooled four-element *e*-beam source at 45° to the sample, was deposited at 10^{-7} Pa onto this maximally ordered Ge(001)-$(M \times N)$/Si(001)-(2×1) surface either by reactive-deposition epitaxy (RDE) at 773 K or by SPE at 500 K followed by an anneal at 773 K. Modifications to the Ge(001)-$(M \times N)$ surface due to exposure to the flux of Co atoms at the 773 K growth temperature were monitored in real time, initially by STM and at the later stages, because of the tip shadowing effect, by RHEED. RHEED patterns (9–15 kV) were recorded parallel to the $\langle 100 \rangle$ and $\langle 110 \rangle$ azimuths relative to the Si(001) surface directions.

III. RESULTS

A. RDE of Co on Ge(001)-($M \times N$)/Si(001)-(2×1)

Figure 1 shows the evolution of the initial Si surface after the Ge layer growth and subsequent exposure to the flux of Co atoms at 773 K. As can be judged from Fig. 1(a), the initial surface is a well-ordered, atomically flat Si(001) surface, (2×1) and (1×2) reconstructed, as deduced from smaller area STM observations and from the RHEED pattern in the inset [blown up in Fig. 6(a)].[29] The Ge(001)-$(M \times N)$ shown in Fig. 1(b) layer is also of comparable quality, although of course, it contains two types of vacancy line defects (that appear as dark fringes in the STM image) causing $(M \times N)$ periodicity and streak splitting in the RHEED pattern in the inset[29] [indicated by short white lines in Fig. 6(b)]. It is important to note that this Ge wetting layer is absolutely flat and shows no 3D islands at this stage. Therefore, the appearance of 3D islands, in the form of bright nanometer-size protrusions, such as the one shown in Fig. 1(c), immediately after opening the Co-evaporator shutter could be directly attributed to the interaction of Co with the Ge layer. Equally striking is the change of the RHEED pattern from a 2D to a 3D chevron-type pattern [see inset in Fig. 1(c), and Fig. 6(c)], characteristic of faceted nanocrystals, such as the Ge pyramids and huts.[29] Comparison between this RHEED pattern in Fig. 6(c) and a pattern from pure Ge nanocrystal-covered surface [from a different set of Ge–Si(001) growth experiments[25–29] shown in Fig. 6(d)] reveals close similarity in the shape of {111} and {002} reflections and the arrowhead shape of the {113} reflections, as well as in the zigzag shape of the half-order streaks pointed to by

white arrows. Close examination of these nanoprotrusions (Fig. 2) reveals that they are composed of two different types of nanocrystal: elongated ones situated diagonally (parallel to the ⟨110⟩ substrate directions) at the crests of the underlying pyramidal ones (with the sides parallel to the ⟨100⟩ directions). Hence, the pyramids at the bottom, as outlined in Fig. 2(b) and 2(d), are undoubtedly Ge nanocrystals responsible for most of the zigzag or chevron RHEED pattern. The elongated features at the Ge nanocrystal tops, most probably Co-containing germanides, were the ones to contribute to the RHEED pattern in Fig. 1(c) the four spots at the quarter-order positions, marked by black arrows in Fig. 6(c).

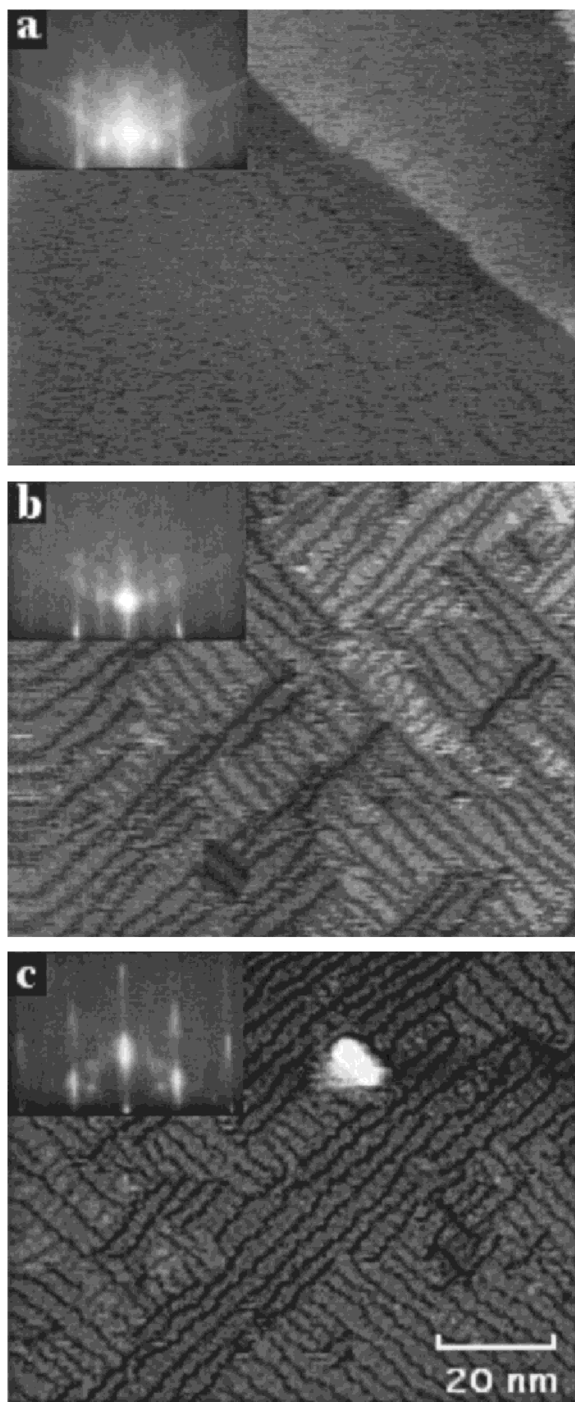

FIG. 1. Constant-current STM images showing the evolution of the (a) initial Si(001)-(2 × 1) surface after (b) gas source MBE of Ge(001)-($M \times N$)–Si(001)-(2 × 1) and (c) reactive-deposition epitaxy of Co/Ge(001)-($M \times N$)/Si(001)-(2 × 1) at 773 K. (a,b) −1.5 V, 0.08 nA, (c) −4.0 V, 0.08 nA. RHEED patterns (12 kV) in the insets correspond to Si ⟨110⟩ azimuth (dimer row and step directions).

Scanning tunneling *I–V* spectra (STS) were then acquired from both nanocrystal types, as well as from the surrounding Ge(001)-($M \times N$) layer. The results are shown in Fig. 3: although all the spectra exhibit rectifying behavior, there are, nevertheless, recognizable differences between them, suggesting the different nature of the three substances.

B. Solid-phase epitaxy of Co on Ge(001)-($M \times N$)/Si(001)-(2 × 1)

The Ge(001)-($M \times N$) surface with a few germanide nanocrystals on top of Ge pyramids, obtained by RDE of Co as described in the previous section, served as a substrate for the next set of SPE experiments. Although in a typical SPE experiment metal deposition is performed at room temperature (RT), the temperature for our experiment was set to 500 K. On the one hand, it should be too low to promote phase formation, and on the other hand, sufficiently high to prevent undesired adsorption onto the sample surface, keeping it atomically clean. The latter consideration is very important, because most STM studies are based on the analysis of surface features, and every effort should be paid to keep any unrelated and irrelevant species away from the surface under investigation. Otherwise, some adsorption onto a surface, especially at RT, may take place with time even under UHV conditions.

The results of Co deposition at 500 K are shown in Fig. 4(a): the entire surface appears to be covered with small bright protrusions. Germanide nanocrystals on top of Ge pyramids from the previous RDE experiment can be clearly distinguished from the rest of the Ge(001)-($M \times N$) substrate, even under this additional Co coverage. The RHEED pattern [in the inset and blown up in Fig. 6(e)] has also changed accordingly, from a chevron-type characteristic of 3D faceted islands to a spot-pattern from transmission through less-defined 3D features, which could be indexed as cubic ⟨110⟩-zone.

After a 1-h anneal at 660 K, reaction and/or growth seem to have taken place, because the small protrusions increase in size and become elongated [see Fig. 4(b)]. This change modified the reciprocal space accordingly, manifested in the corresponding RHEED pattern in the inset [also cf. Fig. 6(f)]. Yet another change occurs after a prolonged anneal at 673 K, even though it seems not to have affected the diffraction pattern: this time there are rather symmetrical, equiaxed crystallites located at the

troughs of the faceted pyramids [see Fig. 4(c)]. Hence, once more, the reaction caused two types of nanocrystal to appear: pyramids similar to the ones obtained by RDE, with, however, equiaxed rather than elongated second-type nanocrystals, at the pyramid troughs (magnified and outlined in Fig. 5). Figure 6(a)–6(f) summarizes the evolution of RHEED patterns (see text for details). It is important to note that there were no variations in surface periodicity, as measured from interstreak spacings, suggesting full coherency throughout the entire transformation sequence.

The surface morphology after a further 15-h anneal is shown in Fig. 7(a). Although STS spectra from these nanocrystal islands and from the interisland area, shown in Fig. 8, still differ from each other, they both show ohmic behavior (especially at low biases), very different from the rectifying spectra in Fig. 3.

IV. DISCUSSION

A key to understanding the observed morphologies as a function of growth method and heat treatments is the Effective Heat of Formation model (EHF),[30–32] which relates the effective concentration of the metal atoms at the growth interface available to participate in the reaction, with the sequence of phases formed.[33] According to this model, slow metal deposition onto a substrate at high temperature ensures low effective metal concentration at the growth interface. In other words, every metal atom arriving at the surface reacts immediately, and accumulation of metal is avoided. As a result, the first phase formed is not the one with the lowest heat of formation, but the one with the lowest metal content. In metal–silicon systems, it is usually metal disilicide, $MeSi_2$, which is the last phase in the equilibrium diagram. Immediate and direct formation of disilicides in RDE was experimentally confirmed for Co–Si, Ni–Si, and Fe–Si systems.[33] For example, the authors themselves have obtained $CoSi_2$ by RDE at 773 K,[18] about 50 K lower than the SPE $CoSi_2$ formation temperature,[33] and avoiding the intermediate Co_2Si and CoSi phases.

Therefore, it is reasonable to assume that our RDE of Co onto Ge(001)-($M \times N$)/Si(001)-(2×1) layer, which was slow enough and at sufficiently high temperature of 773 K, has led to the formation of cobalt

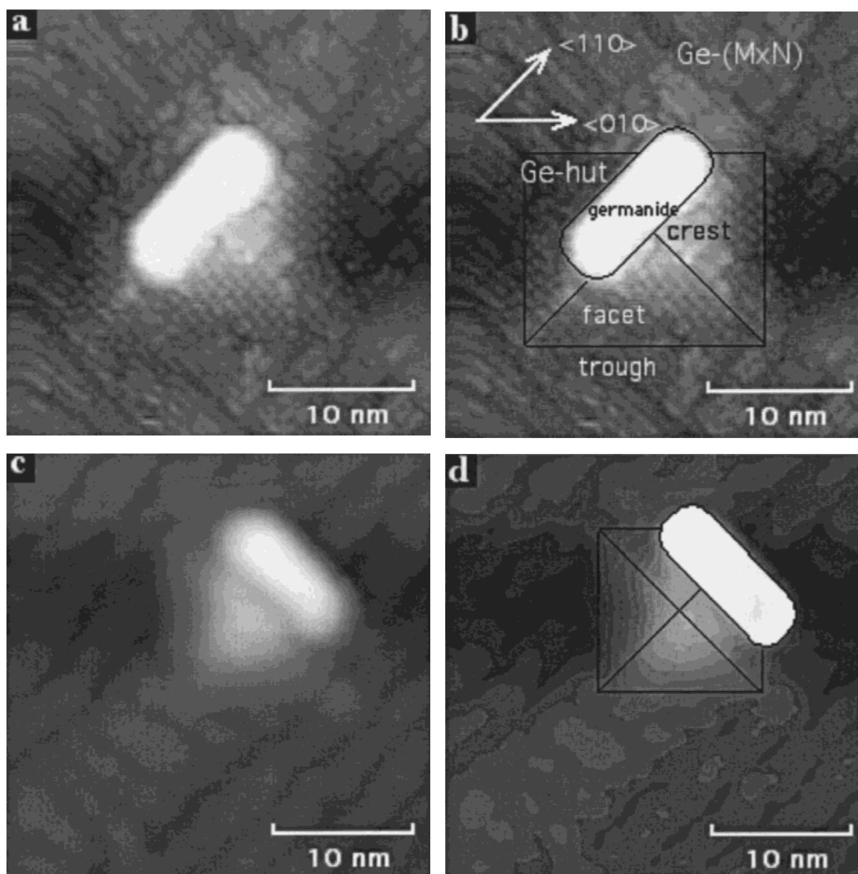

FIG. 2. (a) Atomically resolved constant-current STM magnification of one of the nanocrystals shown in Fig. 1(c) (filled-states: –1.5 V, 0.08 nA). (b) Outline and annotation explaining the features described in the text. Note the location of the elongated germanide nanocrystal (parallel and perpendicular to the dimer row ⟨110⟩ directions) at the crest of the underlying germanium pyramid (at 45° to the dimer row ⟨110⟩ directions), as well as the interisland Ge(001)-($M \times N$) surface. (c,d) Another example, where the germanide is close to the Ge-pyramid crest. (d) Filtered to emphasize the contours of equal height of the pyramid.

digermanide, $CoGe_2$, which is also the last phase in the equilibrium diagram.[15] This orthorhombic phase ($a_{CoGe_2} = b_{CoGe_2} = 5.68$ Å, $c_{CoGe_2} = 10.82$ Å) is thus under 0.35% compression on Ge ($a_{Ge} = 5.66$ Å), if $(001)CoGe_2 \parallel (001)Ge$ (see left-hand side of Fig. 9). However, in our case, the Ge layer is fully strained to the Si lattice constant ($a_{Si} = 5.43$ Å), at least at the Ge(001)-($M \times N$)/Si(001)-(2 × 1) interface. The lattice constant at the top of the Ge layer can be slightly closer to the Ge lattice constant. Hence, the effective mismatch between the $CoGe_2$ and Ge(001)-($M \times N$)/Si(001)-(2 × 1), i.e. at the $CoGe_2$/Ge(001)-($M \times N$) interface, is $0.35\% < \epsilon < 4.2\%$. Thus, a situation arises in which the Ge layer experiences 0.35–4.2% tension at the upper, $CoGe_2$–Ge(001)-($M \times N$), interface, and 4.2% compression at the lower, Ge(001)-($M \times N$)–Si(001)-(2 × 1), interface. $CoGe_2$, on the other hand, experiences 0.35–4.2% compression at the $CoGe_2$/Ge(001)-($M \times N$) interface. The strain can be even larger if, as was found by Mello *et al.*,[3] the *c* variant ($c_{CoGe_2} = 10.82$ Å stretched over two Ge unit cells) is present in the film. This compression should be sufficient to drive the 2D-to-3D transition of the $CoGe_2$, because 3D islands allow for elastic relaxation at their crests,[24] which can account for the formation of the elongated 3D nanocrystals (cf. Fig. 2).

Furthermore, the additional strain exerted by the $CoGe_2$ on the Ge layer, which is already strained to 4.2% at the Ge(001)-($M \times N$)/Si(001)-(2 × 1) interface, apparently lifts the metastability of this pseudomorphic layer, and, in turn, promotes 2D-to-3D transition there. This can explain the formation of the Ge pyramids and huts at the initially flat Ge epilayer, as shown in Figs. 1 and 2. The pyramid STM images in Fig. 2 and

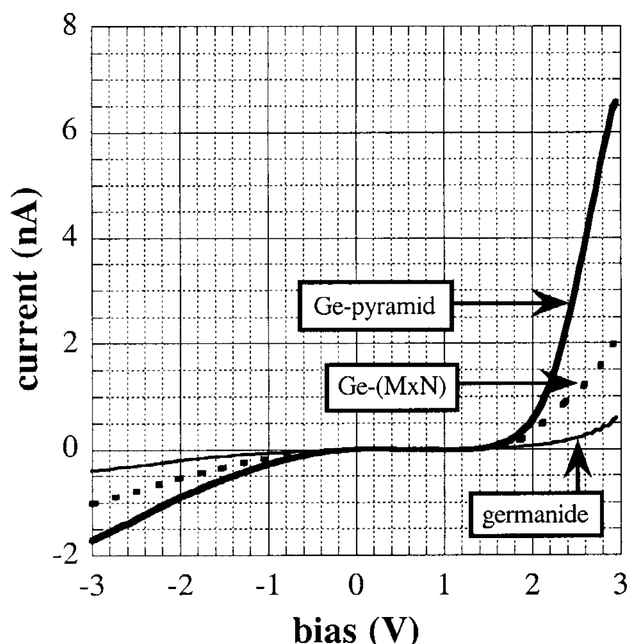

FIG. 3. Scanning tunneling spectra (STS) from the germanide and underlying germanium nanocrystals shown in Fig. 2, as well as from the surrounding Ge(001)-($M \times N$) surface.

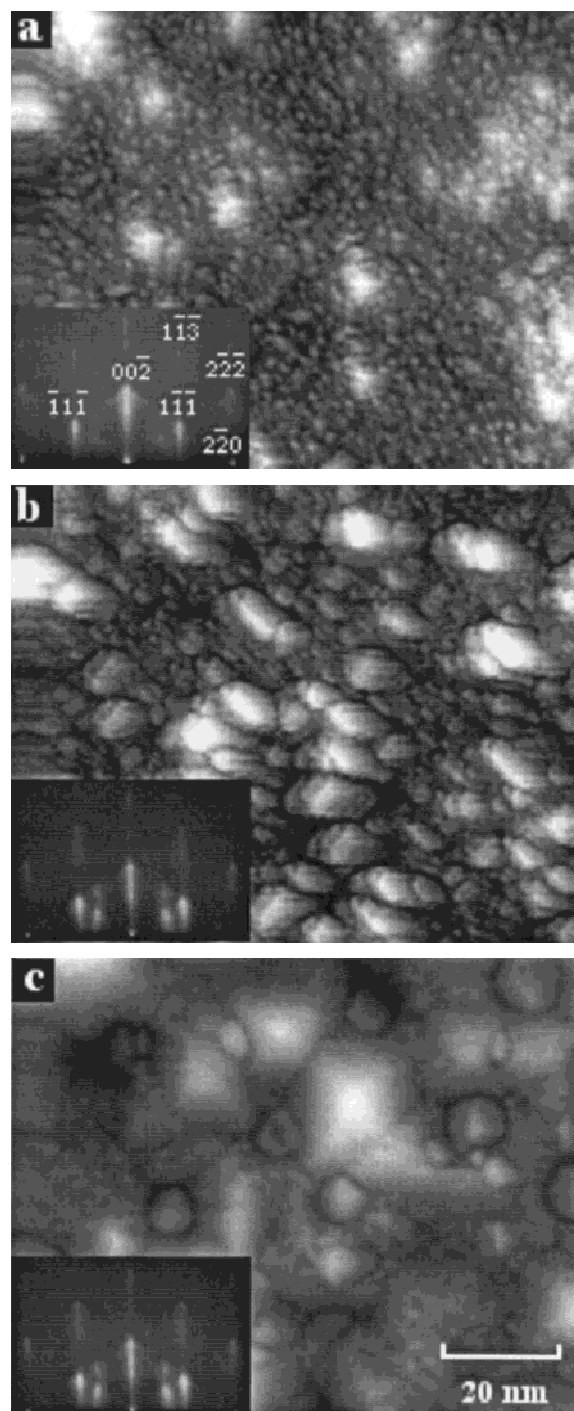

FIG. 4. Constant-current STM images showing the evolution of the Ge(001)-($M \times N$)/Si(001)-(2 × 1) surface after (a) solid-phase epitaxy of Co/Ge(001)-($M \times N$)/Si(001)-(2 × 1) at 500 K, and anneals (b) 1 h at 660 K, and (c) 15 h at 673 K. (a,b) −1.5 V, 0.08 nA, (c) −2.0 V, 0.08 nA. RHEED patterns (12 kV) in the insets correspond to Si ⟨110⟩ azimuth.

their corresponding RHEED patterns in the inset of Fig. 1(c) and Fig. 6(c) are fully consistent with nanocrystals found at the surface of Ge layers grown beyond the Stranski–Krastanow limit [cf. Fig. 6(d)].[24–29] The germanide contribution to the diffraction pattern is the four spots near the shadow edge [indicated by black arrows in Fig. 6(c) and 6(f)], close to the one-fourth order spectral positions, which do not belong to the Ge-hut chevron pattern.[27–29]

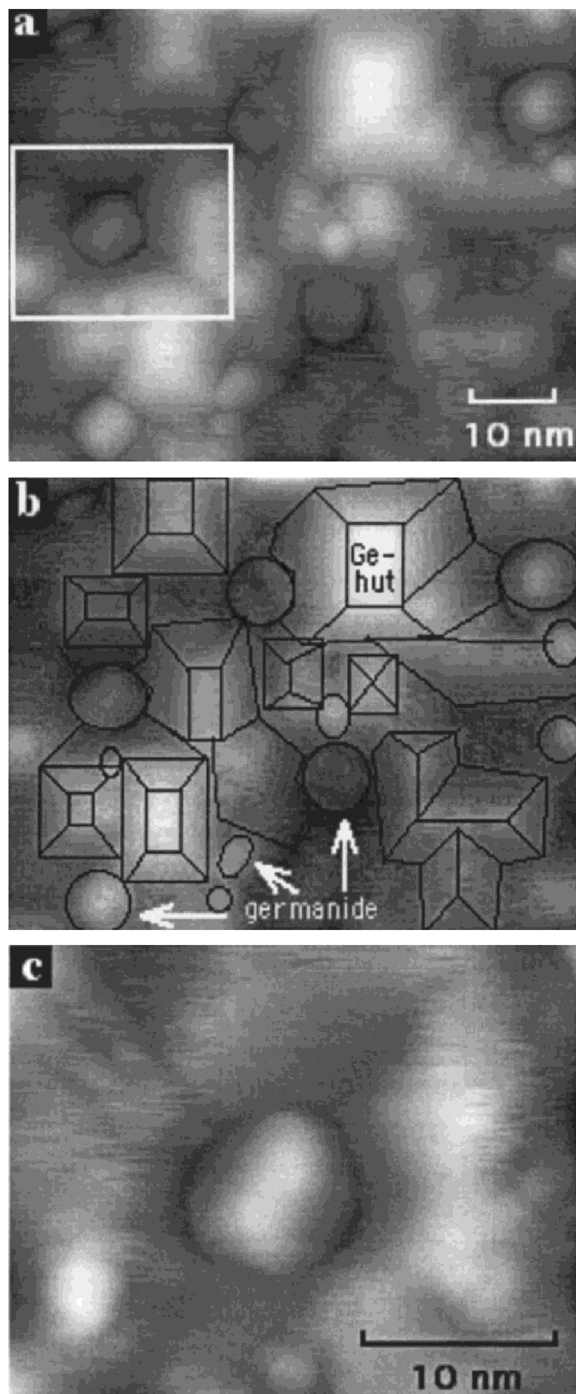

FIG. 5. (a–c) Magnified and outlined constant-current STM image of one of the surfaces shown in Fig. 4(c) (filled-states: –2.0 V, 0.08 nA), to exemplify the relative disposition of the germanide and germanium nanocrystals. (c) Magnification of the framed rectangular region in (a), to show the "nesting" of the equiaxed germanide nanocrystal at the valley made by the troughs of the surrounding germanium pyramids and huts facets.

The relative location of the elongated $CoGe_2$ and pyramidal Ge nanocrystals can also be understood in the framework of strain distribution and relaxation in the layers. Because $CoGe_2$ possesses the larger unit cell of the two, the most "comfortable" location for it would be at the maximally relaxed regions in the vicinity of the pyramid or hut crests. Hence, the most probable scenario consists of the formation of strained $CoGe_2$ nanocrystals, which, by applying additional strain on the Ge wetting layer, lift the layer's pseudomorphism and "pull out" Ge nanocrystals. Existence of 3D cobalt germanide nanocrystals has been implicitly suggested,[7] but not convincingly shown until this work.

EHF states that in the case of solid-phase reaction, when the effective metal concentration at the growth interface is large and/or the substrate temperature is not high enough for the instantaneous reaction, the first phases formed will be richer in metal.[33] Indeed, in the Co–Si system the sequence of phase formation under SPE conditions is Co_2Si, CoSi, and only then $CoSi_2$. In the Co–Ge system, Co_5Ge_7 has been shown by Ashburn *et al.*[1] to be the first phase to form by solid-phase reaction at 573 K, transformed to $CoGe_2$ at 700 K. This can explain

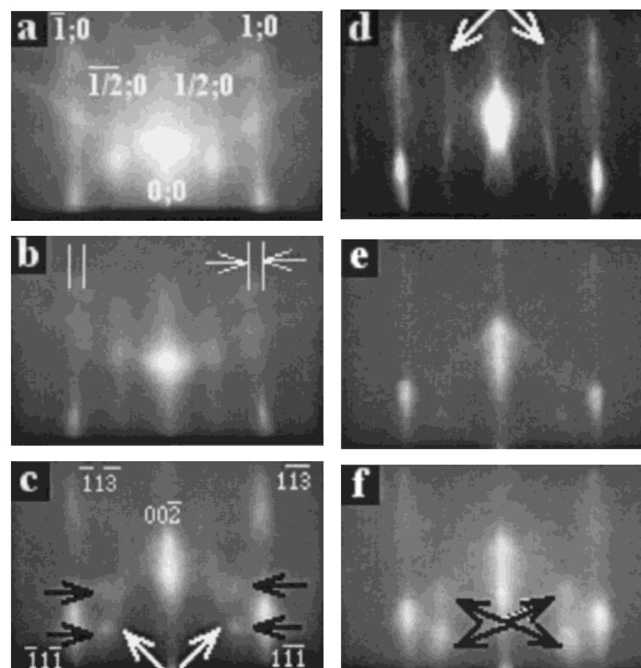

FIG. 6. Surface evolution starting from the (a) initial Si(001), via (b) flat Ge/Se(001), up to (c) Co/Ge/Si(001) by RDE and (e,f) by SPE, as reflected in ⟨110⟩-RHEED patterns. (d) ⟨110⟩-RHEED pattern from clean Ge/Si(001) surface exhibiting hut and pyramid morphology, from different experiments, given here for comparison.

the morphology presented in Fig. 4. Epitaxial Co_5Ge_7 (a = 7.64 Å, c = 5.81 Å), with its (001) surface parallel to the Ge(001) surface and Co_5Ge_7 ⟨100⟩ ∥ Ge ⟨110⟩, would exert 4.5% compression (or even more if the Ge lattice constant is strained to a value close to that of Si) on the underlying Ge(001)-($M \times N$) layer, with Co_5Ge_7 periodicity in ⟨100⟩ crystallographic directions doubles the Ge ⟨110⟩ periodicity (see right-hand side of Fig. 9). Again, this would result in the formation of Co_5Ge_7 and Ge nanocrystals. However, as the Co_5Ge_7 lattice constants are smaller than that of Ge, this time the most "comfortable" location would correspond to the more compressed regions at the Ge pyramid and hut troughs creating a "raisin-cake" appearance, as shown in Fig. 4(c). The magnified image in Fig. 5(a)–5(c) nicely shows and outlines this "nesting" of the germanide nanocrystals in the troughs formed by the {501} facets of the neighboring Ge huts. The small protrusions in Fig. 4(a) are most probably unreacted Co, which begins to react and form Co_5Ge_7 nanocrystals at 660 K, as shown in Fig. 4(b), with subsequent "pullout" of the Ge pyramid and hut nanocrystals [Fig. 4(c)]. The germanide contribution to RHEED patterns, in the insets of Fig. 4(b), Fig. 4(c), as well as in Fig. 6(c) and 6(f), at this point prevailed over the Ge-hut contribution, as could be concluded from the increased intensity of the four germanide spots, at the expense of the chevron pattern intensity. Further anneal at the close to 700 K temperature caused the Co_5Ge_7 to transform to the final, $CoGe_2$, phase. Again, because of lattice mismatch with Ge, $CoGe_2$ was in a shape of elongated 3D nanocrystals, as shown in Fig. 7(a). In accordance with RHEED, Ge pyramids and huts were not seen anymore in the STM images, either because they were all covered by the germanide nanoclusters or because all the Ge was consumed by that time. The latter seems more likely, because none

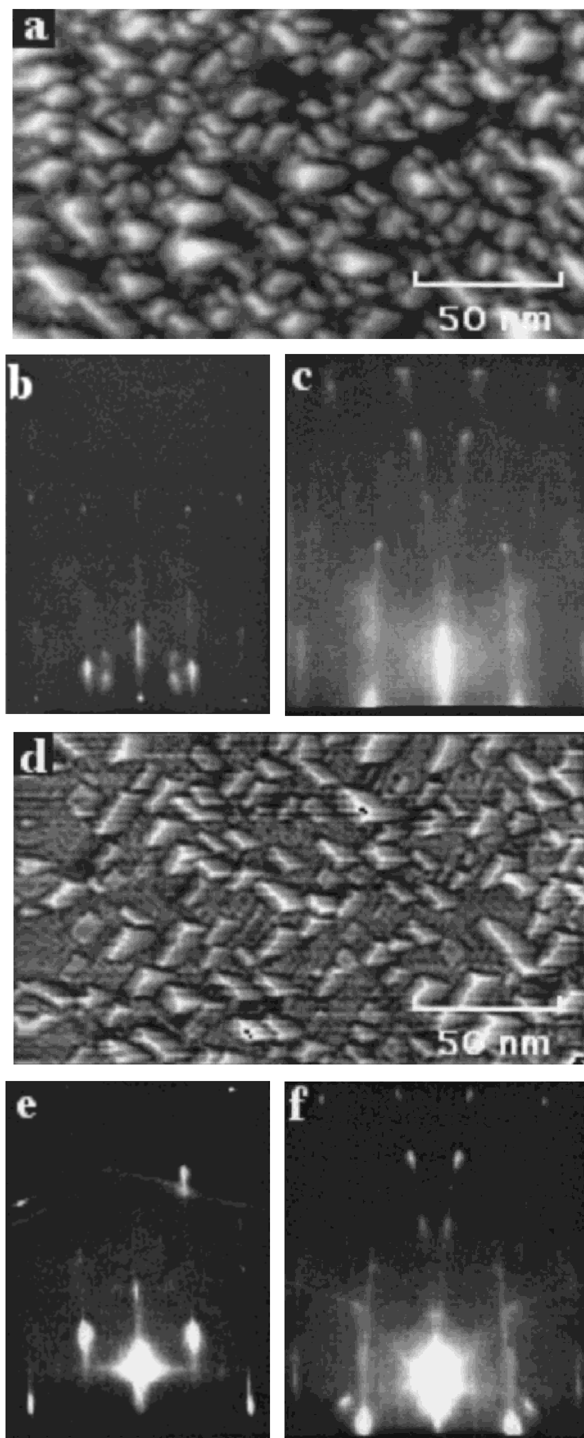

FIG. 7. Constant-current STM images of (a) germanide nanocrystals (−0.5 V, 0.08 nA) with the corresponding (b) ⟨110⟩ and (c) ⟨100⟩ 12 kV RHEED patterns (see text for details). (d) Cobalt disilicide nanocrystals (−4.0 V, 0.08 nA) and the corresponding (e) ⟨110⟩ and (f) ⟨100⟩ 12 kV RHEED patterns are shown for comparison.

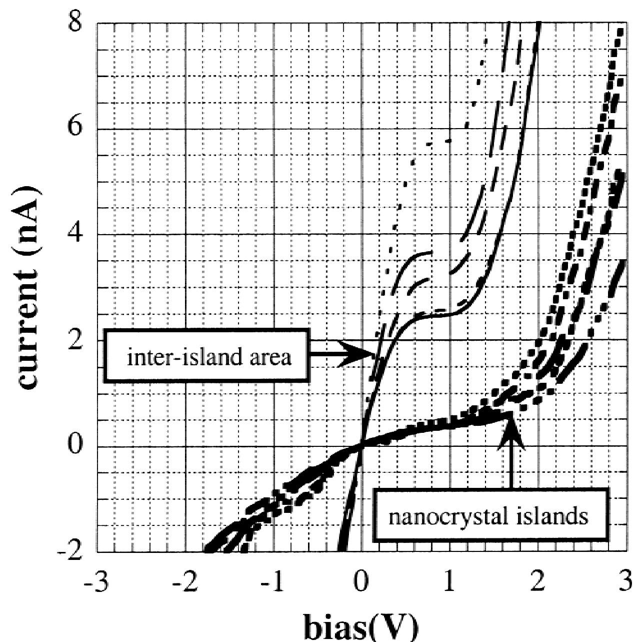

FIG. 8. Scanning tunneling spectra (STS) from the germanide nanocrystal islands (thick) shown in Fig. 6(a) and from the surrounding interisland area (thin lines).

of the *I–V* spectra in Fig. 8 resembled the spectrum from Ge-huts shown in Fig. 3. $CoSi_2$ has been detected at the Co/Ge interface of the Co/Ge/Si sandwich structure by Ashburn *et al.*[1] and by Prabhakaran *et al.*[7,14] and explained by the Co diffusion through Ge layer to preferentially react with Si due stronger Co–Si bonds.[8,10] There are three indications that $CoSi_2$ may, in fact, have been formed in our samples at that point. (i) The surface shown in Fig. 7(a) resembles $CoSi_2$/Si(001) surface shown in Fig. 7(d). Of course, there are similarities, because the size of disilicide and digermanide nanocrystals is comparable, and the elongation directions are parallel to ⟨110⟩. (ii) Although the ⟨110⟩ RHEED pattern in Fig. 7(b), from the surface shown in Fig. 7(a), undoubtedly exhibits germanide reflections, and is not similar to the $CoSi_2$ ⟨110⟩ pattern [compare with Fig. 7(e)], the ⟨100⟩ pattern in Fig. 7(c) exhibits distinct arching of intensity characteristic of $CoSi_2$ [compare with Fig. 7(f)].[18,23] It is, however, possible that the germanide also produces such curved streaks. The origin of the curvature is not clear: although some explanations have been proposed by Stalder *et al.,*[23] our previous work did not agree with them.[18] (iii) Finally, the ohmic STS spectra in Fig. 8 resemble the ones from $CoSi_2$.[18] Hence, even though $CoGe_2$ resistivity is not considerably higher,[1–5] certain presence of $CoSi_2$ in our sample at that final stage could not be ruled out.

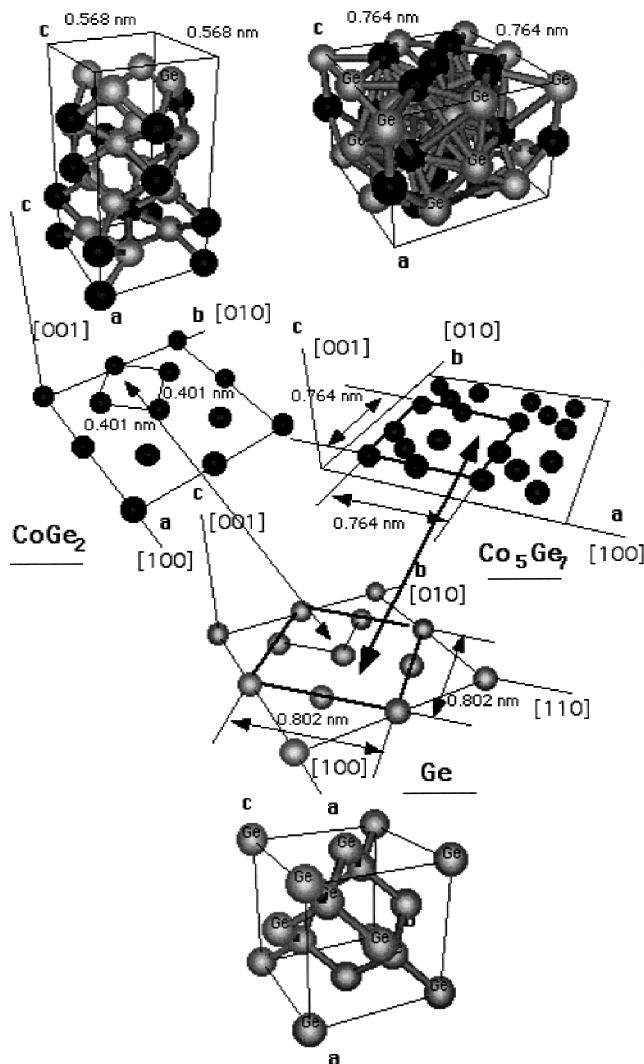

FIG. 9. Schematic drawing of Ge (bottom), $CoGe_2$ (left), and Co_5Ge_7 (right) bulk phases, and their $CoGe_2$(001) ∥ Ge(001) and $CoGe_2$[100] ∥ Ge[100] and Co_5Ge_7(001) ∥ Ge(001) and Co_5Ge_7[100] ∥ Ge[110] matching possibilities. The long thin arrow connects the unit cells for $CoGe_2$(001) ∥ Ge(001) matching, and long thick arrow connects unit cells for the respective Co_5Ge_7(001) ∥ Ge(001) matching.

V. SUMMARY

Although the wide interest in metal-semiconductor compounds stems from their useful properties as contacts and interconnects in very large scale integration (VLSI) technology, there is another side to them that has not been sufficiently explored so far. This side is related to the morphology of metal-semiconductor epilayers, which is determined by a complicated interplay between metal-semiconductor crystalline mismatch, metal-semiconductor interface energy, and surface energy of the metal-semiconductor compound phase. These parameters can be exploited to create 3D nanocrystal arrays on semiconductor surfaces in a controlled manner for nanotechnological applications, which has been our motivation for this research.

Another degree of freedom is added to the equation if the metal is reacted not with a bulk substrate but with a thin pseudomorphic layer on the substrate, as in the case of an interlayer strain coupling to that of the metal-semiconductor phase. That is why we reacted Co with a Ge layer on Si(001), rather than with a Ge(001) substrate. The results proved fascinating. Reactive-deposition epitaxy of Co onto Ge/Si(001) epilayer resulted in the formation of elongated cobalt germanide nanocrystals, which, in turn, caused Ge nanocrystals to form at the initially flat layer, with the germanide nanocrystals located at the crests of the Ge ones. Solid-phase epitaxy of Co onto Ge/Si(001) led to similar results with, however, equiaxed germanide nanocrystals at the Ge nanocrystal troughs. After prolonged anneal, these equiaxed nanocrystals underwent shape transition into elongated ones.

To interpret these results, we used scanning tunneling microscopy and spectroscopy, reflection high-energy electron diffraction, and the Effective Heat of Formation model. It was concluded that $CoGe_2$ was formed as a result of reactive-deposition epitaxy, whereas Co_5Ge_7 resulted from solid-phase reaction first, and only later transformed to $CoGe_2$ by prolonged anneal at elevated temperature. Strain–relaxation in the germanium and germanide layers accounted for their three-dimensional nature, as well as for their relative disposition; with the

smaller-lattice Co_5Ge_7 at the Ge-hut troughs, and larger-lattice $CoGe_2$ at their crests.

More intense experimental and theoretical efforts are required to understand and to model such complex materials systems and processes. For example, advanced equipment with high-spatial resolution and sensitivity, allowing determination of chemical composition of individual nanocrystals with sufficient precision (so-called "nanoprobes"), is imperative. Because in the meantime the only information that can be obtained from individual nanocrystals *in situ* is scanning tunneling I–V spectroscopy, quantitative interpretation of such spectra can be very useful, because their derivative is proportional to the density of states. However, such an analysis requires massive theoretical modeling. Considerable theoretical efforts, e.g., large-scale thermodynamics and elasticity, are also needed to calculate the energies and strain distribution in relevant layered structures and to model the resultant morphologies, and state-of-the-art diffraction equipment to measure and verify these strains. Nevertheless, this work shows certain ability to design surface morphologies based on strain considerations. The need to "tailor" surface nanostructure is facilitated by future devices where nanometer-scale effects will be of paramount importance.

ACKNOWLEDGMENT

This work is supported by Engineering and Physical Sciences Research Council grant (EPSRC GR/M54032).

REFERENCES

1. S.P. Ashburn, M.C. Öztürk, G. Harris, and D.M. Maher, J. Appl. Phys. **74,** 4455 (1993).
2. K.E. Mello, S.R. Soss, S.P. Murarka, T-M. Lu, and S.L. Lee, J. Appl. Phys. **68,** 1817 (1996).
3. K.E. Mello, S.P. Murarka, T-M. Lu, and S.L. Lee, J. Appl. Phys. **81,** 7261 (1997).
4. S. Dhar and V.N. Kulkarni, Thin Solid Films **333,** 20 (1998).
5. Ch. Krontiras, S.N. Georgat, S. Sakkopolous, E. Vitoratos, and J. Salmi, J. Phys.: Condens. Matter **2,** 3323 (1990).
6. C.S. Lee, I.H. Wilson, W.Y. Cheung, Y.J. Chen, J.B. Xu, and S.P. Wong, Nucl. Instrum. Methods Phys. Res. Sect. B **148,** 604 (1999).
7. K. Prabhakaran, K. Sumimoto, and T. Ogino, Appl. Phys. Lett. **68,** 1241 (1996).
8. F. Lin, G. Sarkona, M.K. Hatalis, A.F. Cserhati, E. Austin, and D.W. Greve, Thin Solid Films **250,** 20 (1994).
9. M. Glück, A. Schüppen, M. Rösler, W. Heinrich, J. Hersener, U. König, O. Yam, C. Cytermann, and M. Eizenberg, Thin Solid Films **290,** 549 (1995).
10. Z. Wang, D.B. Aldrich, Y.L. Chen, D.E. Sayers, and R.J. Nemanich, Thin Solid Films **290,** 555 (1995).
11. P.T. Goeller, B.I. Boyanov, D.E. Sayers, and R.J. Nemanich, Thin Solid Films **320,** 206 (1998).
12. B.I. Boyanov, P.T. Goeller, D.E. Sayers, and R.J. Nemanich, J. Appl. Phys. **86,** 1355 (1999).
13. K. Prabhakaran and T. Ogino, Appl. Surf. Sci. **121/122,** 213 (1997).
14. K. Prabhakaran, K. Sumitomo, and T. Ogino, Surf. Sci. **421,** 100 (1999).
15. ASM Handbook, *Alloy Phase Diagrams* (ASM International, The Materials Information Society, 1992), Vol. 3, pp. 2–142; M. Hansen and K. Anderko, *Constitution of Binary Alloys* (McGraw-Hill, New York, 1958), pp. 475–476.
16. W.B. Pearson, *Pearson's Handbook of Crystallographic Data for Intermetallic Phases* (ASM, Metals Park, Ohio, 1985), pp. 1770–1771.
17. V. Scheuch, B. Voigtländer, and H.P. Bonzel, Surf. Sci. **372,** 71 (1997).
18. I. Goldfarb and G.A.D. Briggs, Phys. Rev. B **60,** 4800 (1999).
19. R.T. Tung, J.M. Gibson, and J.M. Poate, Appl. Phys. Lett. **42,** 888 (1983).
20. R.T. Tung and F. Schrey, Appl. Phys. Lett. **54,** 852 (1989).
21. D.P. Adams, S.M. Yalisove, and D.J. Eaglesham, J. Appl. Phys. **76,** 5190 (1994).
22. V. Buschmann, M. Rodewald, H. Fuess, G. Van Tendeloo, and C. Schäffer, J. Cryst. Growth **191,** 430 (1998).
23. R. Stalder, C. Schwarz, H. Sirringhaus, and H. von Känel, Surf. Sci. **291,** 355 (1992).
24. Entire issue no. 4 of the MRS Bull. **21,** 31 (1996) and references therein.
25. I. Goldfarb, P.T. Hayden, J.H.G. Owen, and G.A.D. Briggs, Phys. Rev. Lett. **78,** 3959 (1997).
26. I. Goldfarb, P.T. Hayden, J.H.G. Owen, and G.A.D. Briggs, Surf. Sci. **394,** 105 (1997).
27. I. Goldfarb, J.H.G. Owen, D.R. Bowler, C.M. Goringe, P.T. Hayden, K. Miki, D.G. Pettifor, and G.A.D. Briggs, J. Vac. Sci. Technol., A **16,** 1938 (1998).
28. I. Goldfarb and G.A.D. Briggs, Recent Res. Dev. Mater. Sci. **1,** 189 (1998).
29. I. Goldfarb and G.A.D. Briggs, Surf. Sci. **433–435,** 449 (1999).
30. R. Pretorius, Mater. Res. Soc. Symp. Proc. **25,** 15 (1984).
31. R. Pretorius, A.M. Vredenberg, F.W. Saris, and R. De Reus, J. Appl. Phys. **70,** 3636 (1991).
32. R. Pretorius, T.K. Marais, and C.C. Theron, Mater. Sci. Eng., R **10,** 1 (1993).
33. A. Vantomme, D. Degroote, J. Decoster, C. Langouche, and R. Pretorius, Appl. Phys. Lett. **74,** 3137 (1999).